 doi:10.20944/preprints202011.0652.v1

Article

Hypersonic imaging and emission spectroscopy of hydrogen and cyanide following laser-induced optical breakdown

Christian G Parigger [1,*], Christopher M Helstern [1] and Ghaneshwar Gautam [2]

[1] Physics and Astronomy Department, University of Tennessee, University of Tennessee Space Institute, Center for Laser Applications, 411 B.H. Goethert Parkway, Tullahoma, TN 37388, USA; cparigge@tennessee.edu

[2] Fort Peck Community College, 605 Indian Avenue, Poplar, MT 59255, USA; ggautam@fpcc.edu

* Correspondence: cparigge@tennessee.edu; Tel.: +1-931-841-5690

Abstract: This work communicates the connection of measured shadowgraphs from optically induced air breakdown with emission spectroscopy in selected gas mixtures. Laser-induced optical breakdown is generated using 850 mJ and 170 mJ, 6-ns pulses at a wavelength of 1064 nm, the shadowgraphs are recorded using time-delayed 5-ns pulses at a wavelength of 532 nm and a digital camera, and emission spectra are recorded for typically a dozen of discrete time-delays from optical breakdown by employing an intensified charge-coupled device. The symmetry of the breakdown event can be viewed as close-to spherical symmetry for time-delays of several 100 ns. Spectroscopic analysis explores well-above hypersonic expansion dynamics using primarily the diatomic molecule cyanide and atomic hydrogen emission spectroscopy. Analysis of the air breakdown and selected gas breakdown events permits the use of Abel inversion for inference of the expanding species distribution. Typically, species are prevalent at higher density near the hypersonically expanding shockwave, measured by tracing cyanide and a specific carbon atomic line. Overall, recorded air breakdown shadowgraphs are indicative of laser-plasma expansion in selected gas mixtures, and optical spectroscopy delivers analytical insight into plasma expansion phenomena.

Keywords: laser–plasma interactions; plasma dynamics and flow; hypersonic flows; optical emission spectroscopy; hydrogen; cyanide; Abel inversion; astrophysics; white dwarf stars

1. Introduction

Laser-plasma research is experiencing remarkable interest in laser-induced optical breakdown (LIBS) [1], in part due to success in analytical chemistry, in a volley of engineering applications, or in dedicated diagnosis that may extend to technology-driven changes in the medical field. This work is concerned with experiments and analysis of phenomena associated with pulsed, nanosecond radiation: Optical breakdown is accomplished by focusing a laser beam to irradiances above threshold for local lightning or transient plasma generation in gaseous media. For plasma generation with focused nanosecond laser pulses, the initial portion of the laser pulse energy generates optical breakdown and the remaining portion interacts with the evolving plasma. Micro-plasma imaging is of general interest in the laser-induced breakdown experiments, this includes application of LIBS diagnostic in gases and near liquid or solid surfaces. The analysis and interpretation of observed expansion dynamics can be significantly alleviated when including symmetry considerations.

Optical radiation that is well-above optical breakdown threshold in air, hydrogen, and molar 1:1 CO_2:N_2 molar mixture at or near ambient laboratory conditions, causes multiple breakdown spots in focus. One may associate these spots with peaks in computational maps of the focal area, especially when considering a single lens and spherical aberration [2]. As one reduces the irradiance to the threshold values for the gases of interest, the number of separate breakdown spots diminishes down to one. However, there is always a desire to obtain more diagnostic signal, and reasonably repeatable signals that favor use of radiation that is perhaps of the order of one magnitude, or more, above threshold. This work supports occurrence of reasonable spherical symmetry in gas breakdown

Preprints (www.preprints.org) | NOT PEER-REVIEWED | Posted: 25 November 2020 doi:10.20944/preprints202011.0652.v1

dynamics. Of interest in this work is optical breakdown in air [3], early breakdown phenomena in hydrogen gas [4], and measurement of the diatomic molecule cyanide (CN) [5,6], including spatial distribution for time delays of the order of one microsecond form initiation of optical breakdown.

2. Experimental Arrangement and Methods

2.1. Shadowgraphs

Shadowgraphs of breakdown plasma are used to visualize plasma expansion [3]. It is imperative to capture shadowgraphs for plasma-excitation energies that were used for time-resolved spectroscopy. A Q-Switched neodymium-doped yttrium aluminum garnet Nd:$Y_3Al_5O_{12}$ (Nd:YAG) laser (Quantel model Q-smart 850, USA) is operated at fundamental wavelength of 1064 nm and a 10 Hz repetition rate to deliver full-width-at-half-maximum (FWHM) 6 ns laser radiation with an energy of 850 mJ per pulse. Beam splitters and apertures were used to attenuate laser-pulse energy from 850 to 170 mJ per pulse. Additionally, another Q-Switched Nd:YAG laser (Continuum Surelite model SL I-10, USA) was frequency-doubled to operate at its second harmonic wavelength, 532 nm, with 5 ns pulses.

A 100 mm plano-convex lens, f/10 focusing, is used to focus the 1064 nm IR beam. The 532-nm green laser beam is reflected by two prisms and three mirrors to produce a shadowgraph of the plasma. A beam expander and reflections by the prisms and mirrors caused the beam to become wide enough to cover the entire plasma volume for shadowgraph imaging. Figure 1 shows a schematic of the experimental setup, and Fig. 2 communicates a photograph of a typical shadowgraph experiment.

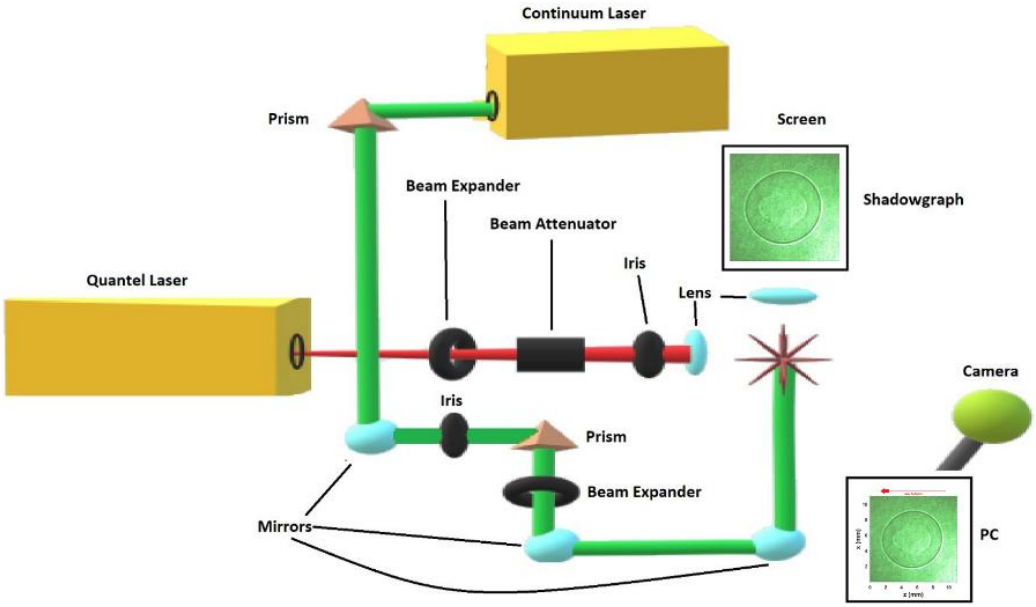

Figure 1. Schematic of the apparatus used for the shadowgraph experiments.

Preprints (www.preprints.org) | NOT PEER-REVIEWED | Posted: 25 November 2020 doi:10.20944/preprints202011.0652.v1

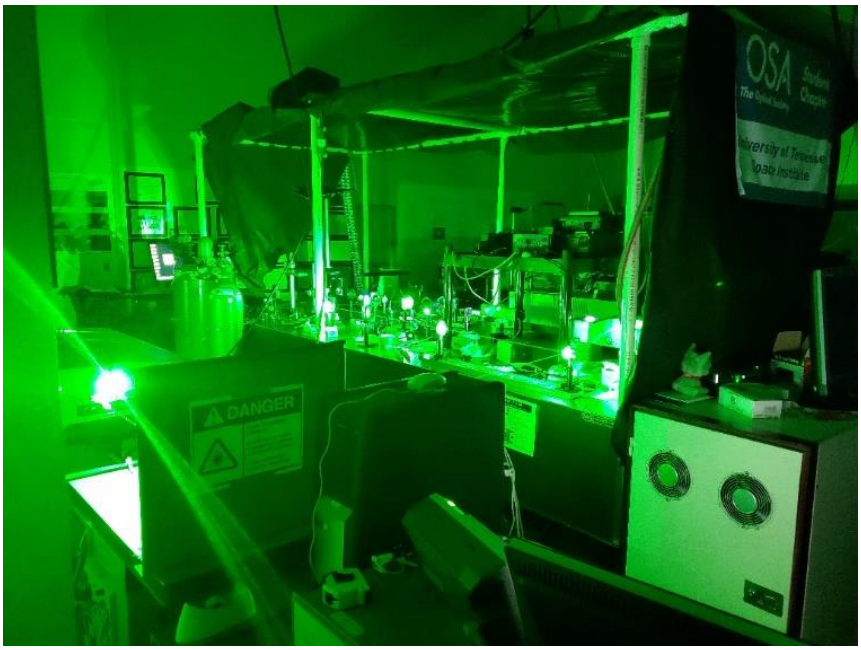

Figure 2. Photograph of the experimental arrangement for air breakdown.

Synchronization of the lasers and camera (Silicon Video Color Camera model 9C10) were performed to ensure precise temporal measurements of shadowgraphs. A control box (TSI Incorporated model 610032, USA), a Digital Delay Generator (Stanford Research System model DG535, USA), and two oscilloscopes were utilized in externally triggering the Surelite laser, Quantel laser, and camera to capture desired shadowgraphs. The externally triggered laser devices had 1-ns RMS amplitude trigger jitter.

Shadowgraphs were recorded using the silicon video camera equipped with a Nikon lens of 50 mm focal length and the silicon video camera was controlled by XCAP imaging software with a PIXCI image capture board. The silicon video camera is equipped with a sensitive area of 6.1 mm × 4.58 mm with a resolution of 3488 horizontal × 2616 vertical pixels or with square 1.75 μm × 1.75 μm pixels image resolution of 512 × 512 pixels was used to capture images by 4 × 4 grouping.

2.2. Emission Spectroscopy

A set of typical components for nanosecond laser-induced breakdown spectroscopy (LIBS) or time-resolved laser-induced optical emission spectroscopy was used in the experimental arrangement [7]. A Q-Switched neodymium-doped yttrium aluminum garnet, Nd:$Y_3A_{15}O_{12}$ (Nd:YAG) laser (Quantel model Q-smart 850, USA) is operated at fundamental wavelength of 1064 nm and a 10 Hz repetition rate to deliver full-width-at-half-maximum (FWHM) 6 ns laser radiation with an energy of 850 mJ per pulse. Beam splitters and apertures were used to attenuate laser-pulse energy from 850 to 170 mJ per pulse. Energy per pulse is measured using the energy and optical power meter (Thorlabs model PM100USB, USA). A silicon photodiode detector (Thorlabs model DET10A/M, USA) is connected to a four- channel oscilloscope (Tektronix model TDS 3054, USA) to measure optical pulses from scattered laser radiation. Alignment of the laser beam is done with three IR reflective mirrors (Thorlabs model NB1-K13, USA) to ensure the laser beam is parallel to the spectrometer slit. A singlet lens (Thorlabs model LA-1509-C, USA) was used to produce optical-breakdown micro-plasma. A fused silica planoconvex lens (Thorlabs model LA4545, USA) was used for 1:1 imaging of the plasma onto the 100 μm slit of a Czerny-Turner type spectrometer (Jobin Yvon model HR 640, Fr) with a focal length of 0.64 nm. The Czerny-Turner type spectrometer has a spectral

Preprints (www.preprints.org) | NOT PEER-REVIEWED | Posted: 25 November 2020 doi:10.20944/preprints202011.0652.v1

resolution of 0.1 nm and is equipped with a 1200 groove/mm grating to disperse the radiation from the plasma into numerous wavelengths. Figure 3 illustrates a schematic of the experimental setup.

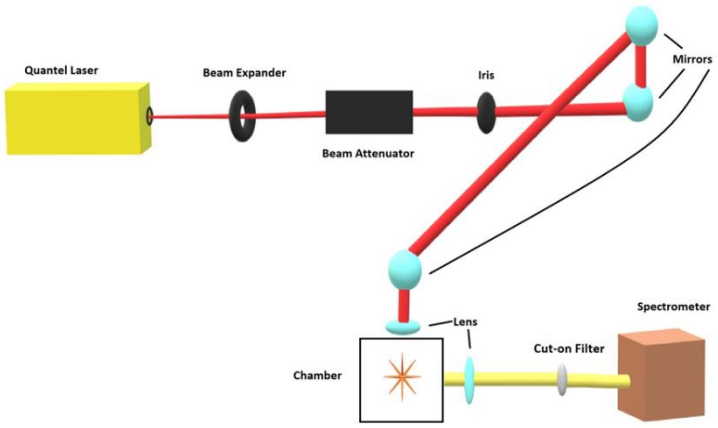

Figure 3. Schematic of the apparatus used for the laser-induced breakdown experiments.

Laser-induced breakdown was created in a controlled gas chamber. The chamber consists of six 0.5-inch diameter and 1 cm thick uncoated uv-fs glass optical windows, two gas inlets, and one gas outlet. The gas inlets were used to mix Airgas ultra-high purity N_2 and research- grade CO_2 via partial pressure addition. Chamber evacuation was performed before and after experimentation via the gas outlet. A mechanical pump was connected to the gas outlet so the chamber could be evacuated as needed. To minimize contamination, the chamber was evacuated with a mechanical pump to bring the system pressure down to 1 Pa (10 mTorr). Chamber monitoring was performed using a differential pressure gauge. The gauge was operated as an absolute pressure gauge by evacuating the gauge casing volume via the vacuum pump. For these set of experiments the chamber consisted of a 1:1 CO_2:N_2 molar gas mixture held at 101 kPa (760 Torr). Measurements were performed with and without an Order-Sorting Filter (Oriel model 51250, USA) with a cut-on wavelength of 309 nm and transmittance range of 325 nm, to evaluate the C I 193.09 nm atomic carbon line interference [8]. Spatially resolved images were recorded with a 2-dimensional intensified charge coupled device (ICCD; Andor Technology model iStarDH334T-25U-04, USA) along the slit height. The ICCD is mounted to the spectrometer, connected to a computer by USB cable, and run by the Andor Solis 64-bit Acquisition and Analysis software. The ICCD has an array of 1024 × 1024 pixels, which coincide with horizontal-spectral and vertical-spatial variations along the slit height. The pixels are binned in four-pixel tracks along the slit direction, resulting in 256 spectra for each time delay. Recording of measurements with and without the Order-Sorting filter consist of 100 accumulations collected for 21 time-delays at 250 ns steps.

Synchronization of plasma generating instrumentation and data collection equipment was accomplished by using a Function Generator (Wavetek model FG3C, USA), a Digital Delay Generator (Stanford Research System model DG535, USA), a custom-built divide by five circuit, and the previously mentioned four-channel oscilloscope. 50 Hz triangular waves are produced by the wave generator and the divide by five circuit box yields a 10 Hz wave. The digital delay generator and production of 10 Hz wave are used to trigger the flashlamp of the laser and synchronize all other equipment.

2.3. Shockwave Analysis Method

Laser-induced breakdown performed on solid, liquid or gaseous materials produces a small explosion. This explosion, together with the excitation, plasma formation and ablation of material, is accompanied by the surrounding material being fiercely displaced and the production of a

Preprints (www.preprints.org) | NOT PEER-REVIEWED | Posted: 25 November 2020 doi:10.20944/preprints202011.0652.v1

shockwave. The geometry and the evolvement over time of a laser-induced shockwave are dependent on the energy of the laser and the shape of plasma produced.

Blast waves due to nuclear explosions set the foundation for the study of shockwave production and propagation. The vast amounts of energy released in a fixed volume by nuclear explosions compared to normal explosions were examined by Bethe *et al.* [9]. at Los Alamos in 1941 and Taylor [10]. in the United Kingdom in 1950 yielding the theory of a point strong explosion. Studies by John von Neumann [9] and L.I. Sedov [11, 12], which assumed an adiabatic expansion and a sudden release of energy, E, in negligible volume and time, lead to the development of the expansion law of the shock wave,

$$\mathbf{R(\tau)} = \frac{\mathbf{1}}{\boldsymbol{K}}\left(\frac{\mathbf{E\,\tau^{2}}}{\boldsymbol{\rho}}\right)^{\frac{1}{5}}, \tag{1}$$

where R(τ) is the radius of the shockwave at time τ, K is a constant dependent on the adiabatic coefficient of the gas, and ρ is the density of the gas. For studies performed in standard ambient temperature and pressure (SATP) air, K ≈ 1, which is consistent with shadowgraph studies performed by Gautam *et al.* [3]. Allowing K = 1, simplifies Equation (1) to: Energies for laser-induced breakdown for cyanide studies fall within the range of 160-200 mJ. Comparisons of computed blast-wave radii, using Eq. (1) with K = 1, for SATP air and molar cyanide (CN) mixture are seen in Tables 1 and 2. There is minimal variation in shockwave expansion in SATP air versus CN mixture, which would indicate that measured shadowgraphs in air provide an acceptable guide for the CN gaseous mixture.

Table 1. Computed shockwave radii for SATP air and for molar CN mixture, 160 mJ.

τ (ns)	R(mm) for air [ρ = 1.2 kg/m^3]	R(mm) for CN [ρ = 1.63 kg/m^3]
200	1.40	1.31
450	1.93	1.82
700	2.31	2.17
950	2.61	2.45
1200	2.86	2.69
1450	3.09	2.90

Table 2. Computed shockwave radii for SATP air and for molar CN mixture, 200 mJ.

τ (ns)	R(mm) for air [ρ = 1. 2 kg/m^3]	R(mm) for CN [ρ = 1.63 kg/m^3]
200	1.46	1.37
450	2.02	1.90
700	2.41	2.27
950	2.73	2.56
1200	2.99	2.81
1450	3.23	3.04

Another important characteristic of the shockwave is the expansion velocity. The shockwave expansion velocity indicates whether the approximation used in the shockwave expansion law is accurate. Shock wave expansion velocity, v(τ), assuming K ≈ 1, is determined by:

$$\mathbf{v(\tau)} = \frac{\mathbf{2}}{\mathbf{5}}\,\boldsymbol{\tau}^{-3/5}\left(\frac{\mathbf{E}}{\boldsymbol{\rho}}\right)^{1/5} \tag{2}$$

Studies by Harith *et al.* [13] verify that the shockwave expansion law is a great approximation when the shockwave expansion velocity is around Mach numbers Ma ≈ 2. However, this work also discusses applicability of the shockwave radius equation, Equation (1), for velocities with Ma >> 2, see Section 3.3.

Mach numbers, Ma, are calculated using

Preprints (www.preprints.org) | NOT PEER-REVIEWED | Posted: 25 November 2020 doi:10.20944/preprints202011.0652.v1

$$\mathbf{Ma} = \frac{\mathbf{v(\tau)}}{\boldsymbol{c}}, \quad (3)$$

where c is the speed of sound in SATP, 343 m/s. Comparisons of computed shock wave expansion velocities and Mach numbers for energies 160 mJ and 200 mJ, using Equations (2) and (3), for SATP air and molar cyanide (CN) mixture are seen in Tables 3 – 6. Shockwave expansion velocities in air for early time delays (450 ns or less) move at hypersonic speeds (Mach numbers 5 or greater), while at later time delays (greater than 450 ns) the shock wave expansion velocities move at supersonic speeds (Mach numbers 1.3 to 5, inclusive). For the CN mixture, the shockwave expansion velocities move at supersonic speeds except for early time delays of 200 ns or less where they move at hypersonic speeds. Therefore, as time elapses the shockwave expansion law approximation improves [13] as Mach numbers approach Ma ≈ 2 and slower.

Table 3. Computed shockwave velocity for SATP air and for molar CN mixture, 160 mJ.

τ (ns)	v(km/s) for air [ρ = 1.2 kg/m^3]	v(km/s) for CN [ρ = 1.63 kg/m^3]
200	2.80	2.63
450	1.72	1.62
700	1.32	1.24
950	1.10	1.03
1200	0.95	0.90
1450	0.85	0.80

Table 4. Computed shockwave velocity for SATP air and for molar CN mixture, 200 mJ.

τ (ns)	v(km/s) for Air [ρ = 1.2 kg/m^3]	v(km/s) for CN [ρ = 1.63 kg/m^3]
200	2.92	2.75
450	1.80	1.69
700	1.38	1.30
950	1.15	1.08
1200	1.00	0.94
1450	0.89	0.84

Table 5. Computed shockwave Mach numbers for SATP air and for molar CN mixture, 160 mJ.

τ (ns)	Ma for Air [ρ = 1.2 kg/m^3]	Ma for CN [ρ = 1.63 kg/m^3]
200	8.15	7.67
450	5.01	4.71
700	3.84	3.61
950	3.20	3.01
1200	2.78	2.62
1450	2.48	2.34

Table 6. Computed shockwave Mach numbers for SATP air and for molar CN mixture, 200 mJ.

τ (ns)	Ma for Air [ρ = 1.2 kg/m^3]	Ma for CN [ρ = 1.63 kg/m^3]
200	8.52	8.02
450	5.24	4.93
700	4.02	3.78
950	3.35	3.15

Preprints (www.preprints.org) | NOT PEER-REVIEWED | Posted: 25 November 2020 doi:10.20944/preprints202011.0652.v1

1200	2.91	2.74
1450	2.60	2.44

2.4. Electron Density Determination Method

2.4.1. Atomic Carbon Line Interference

Laser-induced breakdown performed on the carbon dioxide and nitrogen gaseous mixture produces a variety of species, which includes C, C^+, C^-, CN^+, CN^-, CNN, CO, CO^+, CO_2, CO_2^+, C_2, C_2^+, C_2^-, CCN, CNC, C_2O, C_3, N, N^+, N^-, NCO, NO, NO^+, NO_2, N_2, N_2^+, N_2^-, NCN, N_2O, N_3, O, O^+, O^-, O_2, and O_2^+ [14]. This work focuses on the analysis of the CN violet-band Δv=0 system that has vibrational bands (0, 0), (1, 1), (2, 2), (3, 3) and (4, 4), which are 388.34 nm, 387.14 nm, 386.19 nm, 385.47 nm, and 385.09 nm respectively. The Czerny-Turner spectrometer equipped with 1200 groove/mm grating is adjusted to the region of interest of 370 nm to 393.5 nm to observe the CN violet band Δv=0 system via the Andor Solis software [8].

In LIBS, first order lines (m = 1) are of interest when performing analysis of LIBS produced spectra, but spectral lines have different orders or modes due to the use of diffraction gratings which follow the equation:

$$\mathbf{d\,\sin(\theta) = m\lambda}\,, \tag{4}$$

where d is the distance between the center of two adjacent slits, θ is the angle at which maxima occur, m is the propagation mode of interest, and λ wavelength of monochromatic light. For example, if a first order (m = 1) spectral line has a wavelength, λ, equivalent to 193 nm, then its wavelength, λ, measured in second order (m = 2) would be 386 nm when using equation (4). Even though the spectrometer is set for the desired region of interest and the CN band heads are well defined, there can be interference from the other species' spectral lines in higher order that are produced by the laser-induced breakdown (LIBS). In the cyanide work, there is overlap of the CI 193.09 nm atomic carbon line in second order and the vibrational band (2, 2) of 386.19 nm.

2.4.2. Line Broadening and Deconvolution

Spectral line broadening of observed plasma is caused by the effect of ions and electrons. Local conditions such as local thermodynamic equilibrium and extended conditions such as the plasma radiation's traversed path as viewed by an observer cause the spectral lines to broaden. Doppler or thermal broadening, natural broadening, and pressure broadening are different types of local effect broadening. Doppler broadening is characterized as a Gaussian profile and is due to the position of the detector or observer relative to the velocity of the atoms or ions within a gas or plasma. Natural broadening is characterized as a Lorentzian profile and occurs due to the uncertainty associated with the lifetime of the excited states and its energy. Lastly, pressure broadening is characterized as a Lorentzian profile and is caused by atoms or other ions neighboring the emitter atom or ion. One example of pressure broadening is Stark broadening, which is caused by the shifting and splitting of spectral lines due to the presence of an external electric field, known as the Stark effect.

Electron number density, n_e, can be determined from the full-width at half maximum (FWHM), $\Delta\lambda_{Stark}$, of the stark-broadened CI 193.09 nm atomic carbon line [15], measured in second order,

$$\mathbf{\Delta\lambda_{Stark}\ (nm) = 2w\,(nm) * n_e\ (10^{17}\ cm^{-3})} \tag{5}$$

where width parameter, w, was extrapolated [15, 16], to be $w \approx 0.0029$ nm or by the Stark shift of the CI 193.09 nm atomic carbon line [15],

Preprints (www.preprints.org) | NOT PEER-REVIEWED | Posted: 25 November 2020 doi:10.20944/preprints202011.0652.v1

$$\boldsymbol{\delta\lambda_{Stark}\,(nm) = d\,(nm) * n_e\,(10^{17}\,cm^{-3})}, \quad (6)$$

where the shift parameter, d, was extrapolated to be [15, 16] d ≈ 0.0029 nm. In order to use Equations (5) and (6) to determine n_e, deconvolution of measured Stark FWHM and Stark shifts must be performed. This is due to the line broadening being largely influenced by Stark broadening, which is typically approximated using a Voigt profile [17]. The convolution of Gaussian and Lorentzian line profiles results in the Voigt profile, therefore using a rough approximation between Gaussian, Lorentzian, and Voigt profile widths,

$$\mathbf{f_V} = \frac{\mathbf{f_L}}{2} + \sqrt{\left(\frac{\mathbf{f_L}}{2}\right)^2 + \mathbf{f_G^2}}, \quad (7)$$

where f_V is the FWHM of the Voigt profile, f_L is the FWHM of the Lorentzian profile, and f_G is the FWHM of the Gaussian profile, can be used to apply deconvolution to the measured line profile. In this dissertation, f_V represents the measured spectral line, f_L represents the Stark FWHM or Stark shift, and f_G represents the spectral resolution of the spectrometer. Therefore, rearranging equation (7) to determine f_L yields:

$$\mathbf{f_L} = \mathbf{f_V} + \frac{\mathbf{f_G^2}}{\mathbf{f_V}}, \quad (8)$$

which can be used in conjunction with Equations (5) and (6) to determine n_e of the CI 193.09 nm atomic carbon line in second order.

2.4.3. Method for Computation of Electron Density

Spectra that were unfiltered had an overlap of the (2, 2) CN band head of 386.19 nm and the second order CI 193.09 nm atomic carbon line, where spectra filtered with the cut-on filter only had the (2, 2) CN band head of 386.19 nm. A peak-fitting Matlab® script [18] was applied to filtered and unfiltered spectra to evaluate CI 193.09 nm atomic carbon line in second-order Stark widths and shifts. A typical intermediate record of the five-peak fitting includes fitted background, a single profile for each of the five bands. Figure 4 illustrates recorded data and the overall 'peakfit.m version 9.0' result that is composed of background and sum of five Gaussians versus wavelength.

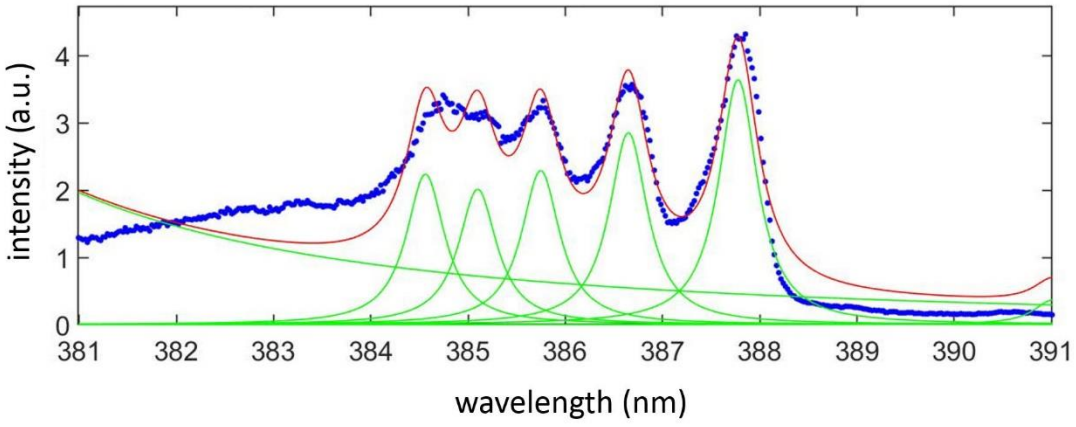

Figure 4. Typical result of the peakfit.m script applied to measured line-of-sight Δv = 0 CN spectra.

Equation (8) was used on the extracted Stark full- width at half maximum (FWHM) and Stark shifts to apply deconvolution. The difference between deconvoluted Stark FWHM from unfiltered spectra and deconvoluted Stark FWHM from filtered spectra was performed to determine the FWHM contribution of the CI 193.09 nm atomic carbon line in second order only. The FWHM contribution of the CI 193.09 nm atomic carbon line in second order only was used in conjunction with Eq. (5) to

Preprints (www.preprints.org) | NOT PEER-REVIEWED | Posted: 25 November 2020 doi:10.20944/preprints202011.0652.v1

determine n_e, where deconvoluted Stark shifts can be used in conjunction with Eq. (6) to determine n_e as well. This communication reports results of n_e from only Stark widths.

2.5. Molecular Spectra Analysis Method

Plasma temperature from molecular spectra is dependent on vibrational and rotational elements of the molecular spectrum. Due to this dependence, temperature from molecular spectra can be used to evaluate the condition of the plasma. Temperature determination can be performed by fitting measured spectra to calculated theoretical diatomic spectrum. Diatomic line strength is used to calculate the needed theoretical diatomic spectrum for appropriate fitting. Diatomic line strength calculations are rather cumbersome to perform due to spectral line position requirements and the need for very accurate molecular rotational constants. Parigger and Hornkohl [19] describe the theoretical background and development of diatomic line strength tables necessary for temperature evaluation. Therefore, cyanide (CN) line strength tables reported by Parigger *et. al* [20] are used for the calculation of theoretical CN spectrum.

The Nelder-Mead temperature (NMT) program [17] was used to fit measured CN spectral data. The NMT program utilizes the Nelder-Mead method [21], which is a numerical method used to find the minimum or maximum of an objective function in a multidimensional space. The NMT program requires initial fit parameter assumptions, which consist of the temperature of the molecular spectra, the line width of the molecular spectral line, and a linear baseline offset. Specifically, the Nelder-Mead algorithm creates a simplex established on the initial given fit parameters. Each vertex of the simplex represents a fit parameter and the size of the simplex is reduced by changing the vertex arrangement until the tolerance is achieved. During minimization, the first local minimum identified represents the minimum and the best fit parameters are established on final location of the simplex's vertices.

2.6. Abel Inversion Method

Determining the information across a plasma allows one to analyze the radial/spatial intensity distribution. Unfortunately, the radial intensity cannot be directly inferred from recorded line-of-sight data. Figure 5 illustrates the line-of-sight experimental geometry. The use of an Abel transform, which analyzes spherically symmetric functions, can be applied to evaluate line-of-sight measurements from close to spherically symmetric plasmas. Specifically, the Abel inversion [22 – 26] technique allows one to extract the radial distributions of electron densities of a close to spherically symmetric plasma directly from the recorded line-of-sight data. Letting $\varepsilon(r, \lambda)$ represent the radial emission coefficient, the Abel transform of $\varepsilon(r, \lambda)$ is shown to be [5, 8, 14, 27 – 30],

$$\mathbf{I(z,\lambda) = 2\int_z^{\rho} \varepsilon(r,\lambda) \frac{r}{\sqrt{r^2 - z^2}}\, dr,} \tag{9}$$

where z is the perpendicular distance from the origin of the line-of-sight, r is the radial distance from the center of the observed plasma at which electron density will be evaluated, R is the radius of the spherical object and ρ is the upper integration limit which is established as being much greater than R, $\rho >> R$. An intensified charge coupling device (ICCD) attached to a spectrometer is used to collect spatial data of the emitted intensity. Line-of-sight spectroscopy usually records spectral radiance; however, it is typical for the LIBS community to use intensity in arbitrary units. An emission intensity map with a function of spatial location and wavelength are displayed by recorded images. Abel inversion is performed on measured line-of-sight data of the emitted spectral intensity and a determination of radial variations is accomplished.

Preprints (www.preprints.org) | NOT PEER-REVIEWED | Posted: 25 November 2020 doi:10.20944/preprints202011.0652.v1

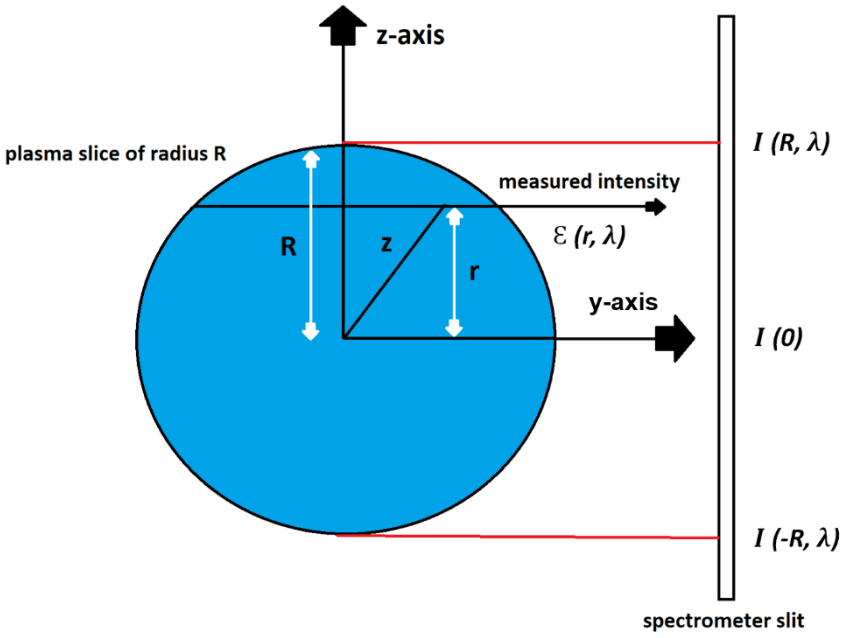

Figure 5. Line-of-sight geometry and Abel inversion method.

The emission intensity has subtle asymmetry along the direction perpendicular to the laser beam which may be a result of laser-plasma interaction that normally takes place in nanosecond laser-induced plasmas or may be a result of variations of the laser pulse profile. Figure 5 displays the geometry of the line-of-sight measurements utilized in this work, where line-of-sight measurements are along the y-axis, the direction of the laser beam is along the z-axis, and the x-axis is perpendicular to the y and z axes. Abel inversion is used to obtain radial dimension measurements of the plasma, which allows for the extraction of plasma radial information. Using the top half and bottom half of line-of- sight profiles subtle asymmetric data points are averaged utilizing the same symmetrization method for atomic hydrogen spectra [27 – 29] and application of Abel inversion is used.

Shadowgraph measurements of plasma kernels in hydrogen and hydrogen-nitrogen gaseous mixtures show a close to cylindrical symmetry or prolate spheroidal symmetry as compared to the close to spherically symmetric plasma kernels in standard ambient temperature and pressure in laboratory air for time delays of 100 to 10,000 ns [3, 28 – 30]. The deviation from close to spherically symmetric plasma kernels may be due to the laser energy employed for laser-induced breakdown, therefore as discussed in this work, shadowgraph measurements in standard ambient temperature and pressure are performed at laser energies observed in the carbon dioxide and nitrogen gaseous mixture, which are seen to be close to spherically symmetric [5]. Due to the spherically symmetric plasma requirement of the Abel inversion technique, collected line-of-sight data is adjusted to allow subtle deviations from circular symmetry and modeled to be spherically symmetric [27 – 29].

Abel inversion of each wavelength determines the spatial distribution and subtle asymmetries present in the captured data are kept by applying an asymmetric factor, which then establish the asymmetric radial distributions [27 – 29]. Pre-treatment of the captured data is not required when using the derivative free Abel inverse transform method [22]. Inversion of Equation (9) can be accomplished using an analytical method with derivatives, known as the Abel inverse transform. Differentiation of spectra is rather challenging; therefore, coefficients are determined by using a complete set of orthogonal polynomials with a minimization method. The use of Chebyshev polynomials in conjunction with the available Matlab® script [22, 26] for Abel inversion of Eq. (9), allows the direct inversion of measured data. For this work, inversion was accomplished by choosing 15 polynomials [22, 23], which maintained fidelity of the spectra and was comparable to the use of a digital filter resulting in computed radial spectra. Smaller spectral resolution would occur with the selection of a smaller number of polynomials. Line-of-sight data along the spectrometer slit were captured and inverted for each wavelength to get the radial intensity distribution. Calibration and

Preprints (www.preprints.org) | NOT PEER-REVIEWED | Posted: 25 November 2020 doi:10.20944/preprints202011.0652.v1

correction for system sensitivity using standard lamps is required for recorded data to undergo Abel inversion and curation of the spectra.

3. Results

3.1. Shadowgraphs

Shadowgraphs of plasma in standard ambient air and temperature (SATP) produced by infrared (IR) 1064 nm radiation with excitation energy of 170 mJ and 6 ns pulse-width are shown below. A single 5 ns pulse-width 532 nm laser beam was used to capture the shadowgraphs. Shadowgraphs were taken in the range of 0.2 to 4.2 μs time delays. Figure 6 displays typical results.

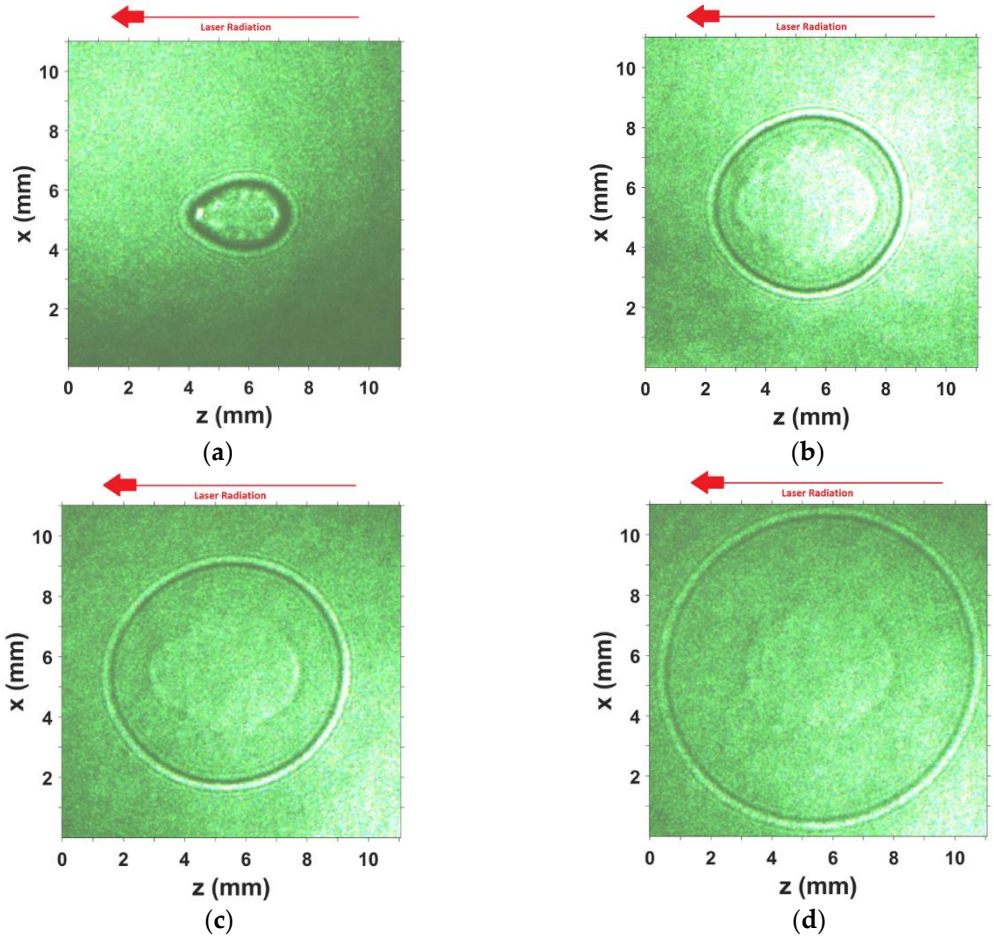

Figure 6. Single-shot shadowgraphs of expanding laser-induced plasma initiated with 170 mJ, 6 ns, 1064 nm pulses, and imaged with 5 ns, 532 nm backlight, time-delayed by (**a**) 200 ns; (**b**) 1200; (**c**) 2200 ns; (**d**) 4200 ns

Further investigations of laser-induced laboratory air breakdown utilize pulse energies of 850 mJ per 6 ns, 1064 nm pulses. Figures 7 and 8 illustrate recorded images in the range of 200 to 4000 ns.

Preprints (www.preprints.org) | NOT PEER-REVIEWED | Posted: 25 November 2020 doi:10.20944/preprints202011.0652.v1

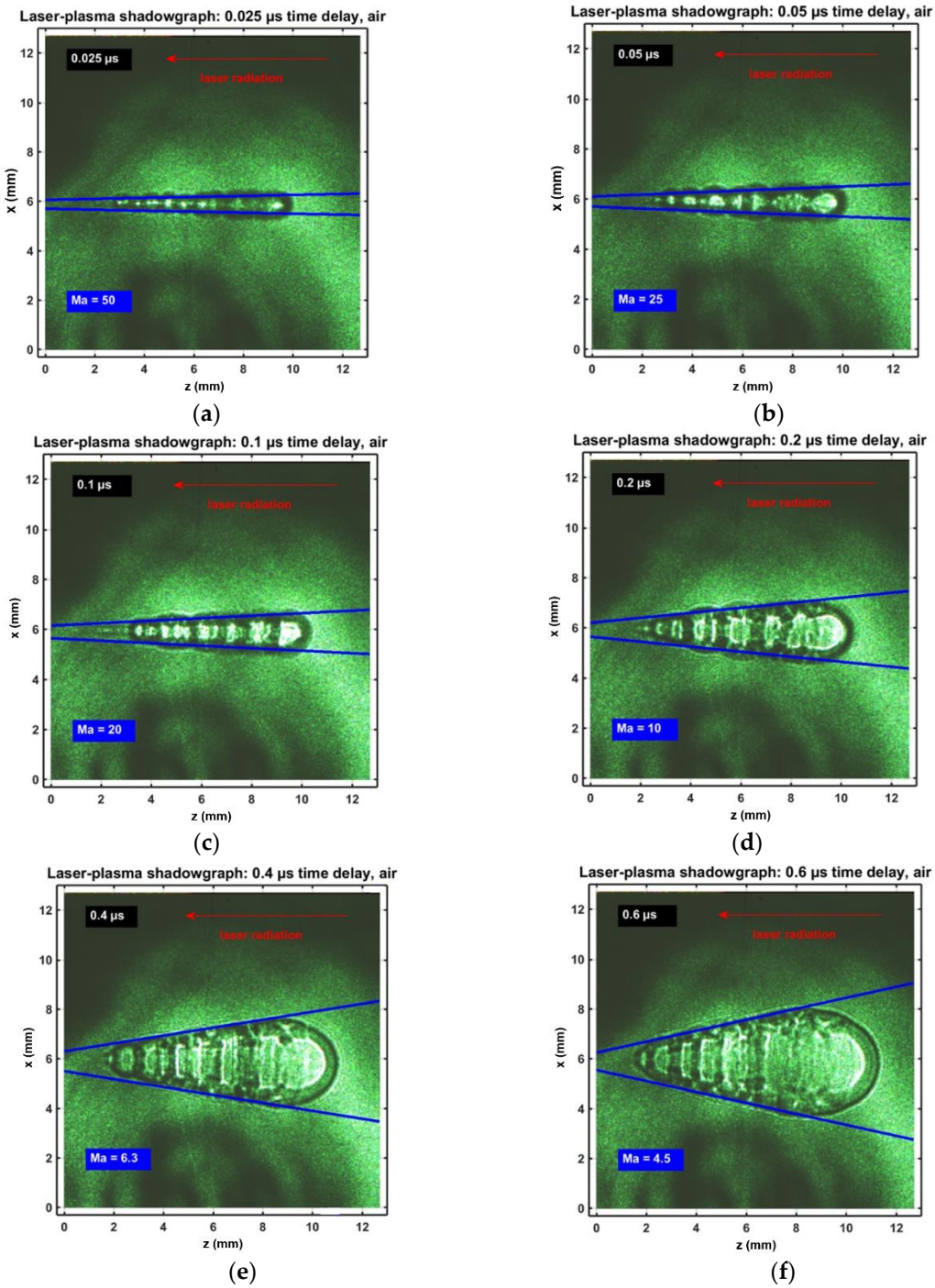

Figure 7. Shadowgraphs subsequent to laser-plasma generation with 850 mJ, 6 ns, 1064 nm pulses. Time delays: (**a**) 25 ns; (**b**) 50 ns; (**c**) 100 ns; (**d**) 200 ns; (**e**) 400 ns; (**f**) 600 ns.

Preprints (www.preprints.org) | NOT PEER-REVIEWED | Posted: 25 November 2020 doi:10.20944/preprints202011.0652.v1

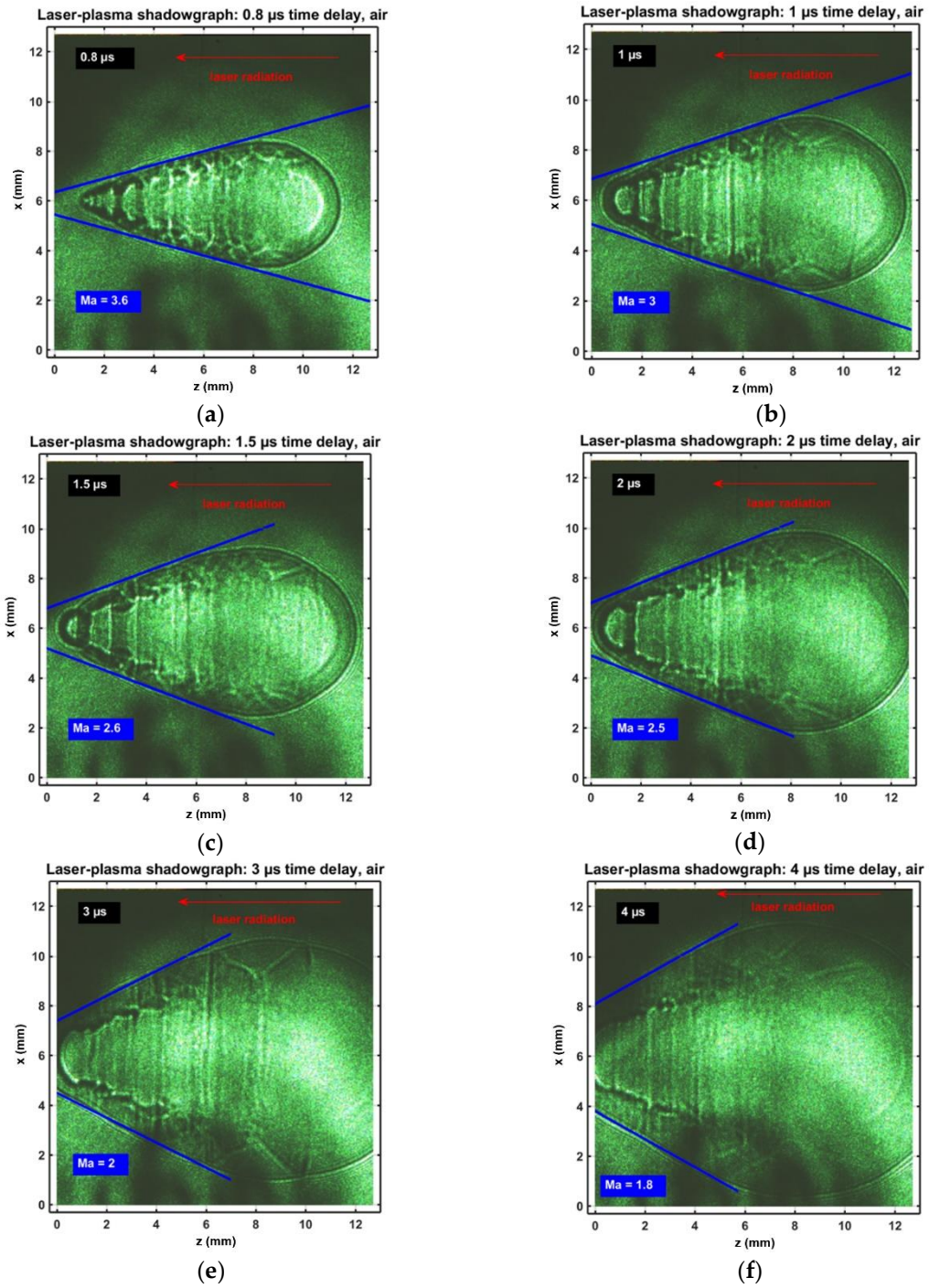

Figure 8. Shadowgraphs captured after laser-plasma generation with 850 mJ, 6 ns, 1064 nm pulses. Time delays: (**a**) 800 ns; (**b**) 1000 ns; (**c**) 1500 ns; (**d**) 2000 ns; (**e**) 3000 ns; (**f**) 4000 ns.

Figures 7 and 8 display multiple breakdown events along the optical axis. Stagnation layers appear to be formed between individual breakdown spots, developing into vertical structures in the forward direction. Stagnation layers have been explored at the interface region of two colliding laser-induced plasmas [31]. The predicted initial plasma expansion speeds in laser-induced optical breakdown are of the order of 100 km/s [32], followed by a gas expansion that is analogous to that of a strong explosion [32]. Figures 7 and 8 also exhibit associated early expansion dynamics that occur at speeds well in excess of hypersonic speeds. The blue lines indicate the forward propagating shockwave boundaries that originate from multiple breakdown spots appearing as 'beads.'

Preprints (www.preprints.org) | NOT PEER-REVIEWED | Posted: 25 November 2020 doi:10.20944/preprints202011.0652.v1

As indicated in Figure 6, the IR 1064-nm, 170-mJ, 6-ns laser beam is along the z axis and moving from the right to left. The expanding shockwave and plasma kernel are clearly visible. At 0.2 μs delay, the plasma kernel appears cylindrical and the expanding shockwave has a prolate spheroidal shape. As time delays approach 1 μs the plasma kernel and expanding shockwave become nearly spherical. As time elapses further, the plasma kernel and expanding shockwave continue to become close to spherical. The vertical extend is about a factor of 1.4 smaller for 170 mJ pulses than that for 850 mJ pulses, according to the Taylor–Sedov energy dependency, Eq. (1), for spherical expansion

3.2. Emission Spectra

The cyanide (CN) spectra captured by the spectrometer and 2-dimensional intensified charge coupled device for a fixed volume of the 1:1 molar CO_2:N_2 gas mixture held at atmospheric pressure are shown in Figure 9. As seen in Fig. 9, the CN violet system $B^2\Sigma^+ - X^2\Sigma^+$ vibrational bands of (0,0), (1,1), (2,2), (3,3) and (4,4) are clearly visible and discernible. The overlap of the CI 193.09 nm atomic carbon line in second order and the (2,2) CN band head is also seen in Fig. 9. At time delays greater than 2.5 μs, the CI 193.09 nm atomic carbon line in second order appears to dissipate and does not overlap the (2,2) CN band head.

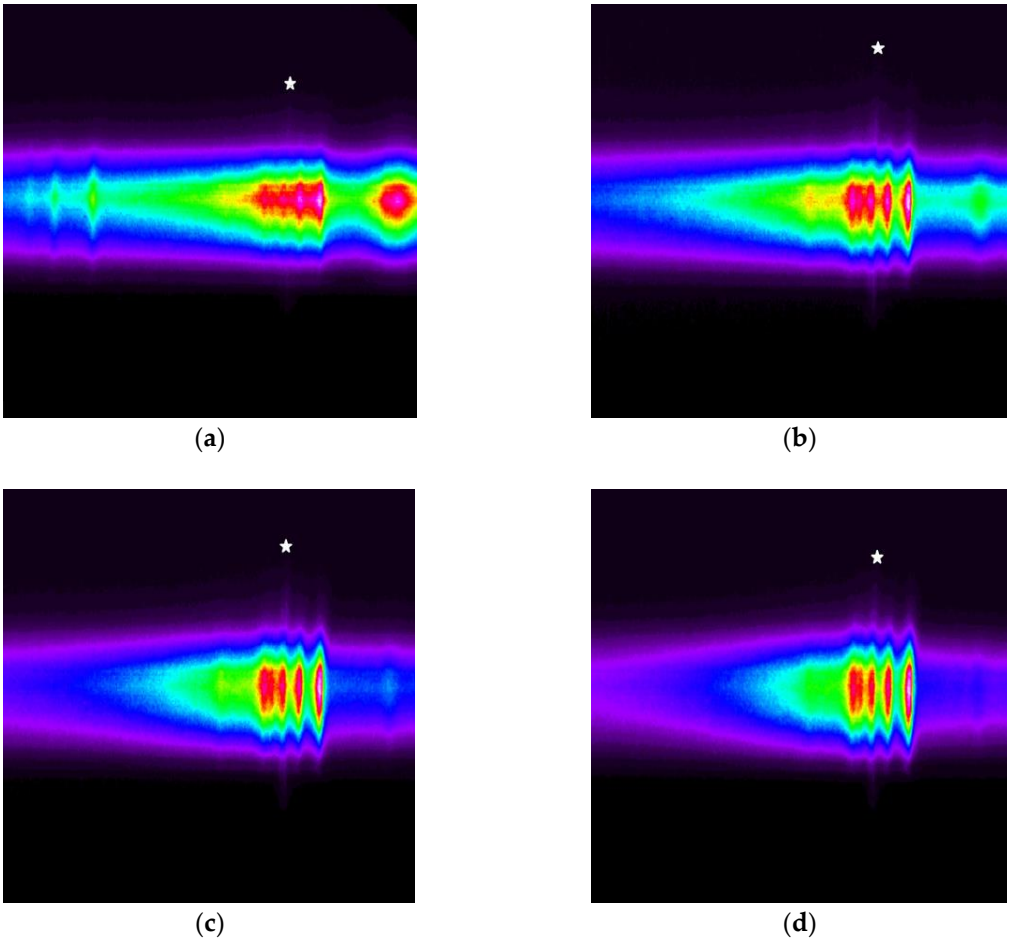

(**a**) (**b**)

(**c**) (**d**)

Figure 9. Optical breakdown CN spectra in a 1:1 molar CO_2:N_2 gas mixture held at atmospheric pressure for time delays of (**a**) 200 ns, (**b**) 450 ns, (**c**) 700 ns, and (**d**) 950 ns. Spectrometer-detector gate width: 125 ns. *, second-order atomic carbon line [5].

In separate experimental runs, CN spectra were captured for a fixed volume of the 1:1 molar CO_2:N_2 gas mixture held at atmospheric pressure with the use of a 309 nm cut-on wavelength filter. The 309 nm cut-on wavelength filter allows for the suppression of the CI 193.09 nm atomic carbon line in second order. Although it is advantageous to apply the 309 nm cut-on wavelength filter for the suppression of the CI 193.09 nm atomic carbon line in second order, the 309 nm cut-on wavelength

Preprints (www.preprints.org) | NOT PEER-REVIEWED | Posted: 25 November 2020 doi:10.20944/preprints202011.0652.v1

filter causes a reduction in spectral intensity captured by the spectrometer and ICCD by ≈ 13%. Filtered and unfiltered spectra also show the CN plasma moving towards the laser as time elapses.

3.3. Shockwave amd Plasma Expansion

The expanding shockwave radii results are shown in Table 7, computed shockwave velocities results are shown in Table 8, and measured plasma kernel radii are shown in Table 9. The expanding shockwave radius for 0.2 μs delay is not exactly consistent with the previously discussed shockwave expansion law, Equation (1), and this can be due to the velocity of the shockwave being greater than the Mach 2 maximum velocity requirement of the shockwave expansion law. For time delays approaching 1 μs and later, the expanding shockwave radii are consistent with the shockwave expansion law, with their shockwave expansion velocities, v(τ), being closer to Mach 2 and slower.

As previously discussed, shockwave expansions in SATP air appear similar in the CN mixtures used in this work. Therefore, the visualization of these shockwave expansions in SATP air provide a good model to the shockwave expansion behavior and plasma kernel geometry in the CN mixtures.

Table 7. Computed shockwave radii versus measured shockwave radii for SATP air, 170 mJ.

τ (ns)	Computed R(mm)	Measured R(mm)
200	1.41	1.00 ± 0.30
1000	2.69	2.67 ± 0.80
1200	2.90	2.83 ± 0.85
2200	3.69	3.57 ± 1.07
4200	4.78	4.95 ± 1.49

Table 8. Inferred shockwave velocities and Mach numbers for SATP air, 170 mJ.

τ (ns)	Velocity, v (km/s)	Mach number, Ma
200	4.03 ± 1.21	11.76 ± 0.30
1000	1.31 ± 0.39	2.67 ± 0.80
1200	1.08 ± 0.32	2.83 ± 0.85
2200	0.58 ± 0.17	3.57 ± 1.07
4200	0.30 ± 0.09	4.95 ± 1.49

Table 9. Measured plasma kernel radii for SATP air, 170 mJ.

τ (ns)	Measured r (mm)
200	0.45 ± 0.13
1000	2.25 ± 0.67
1200	2.40 ± 0.72
2200	3.00 ± 0.90
4200	4.04 ± 1.21

The images recorded for 850 mJ laser-induced plasma generation are also analyzed using the Taylor-Sedov theory of blast wave propagation from a point explosion yields the time dependent radius, $R(t)$, of the shock front [27 – 29],

$$R(\tau) = \xi\,(E/\rho)^{\frac{1}{n+2}}(\tau)^{\frac{2}{n+2}} \sim (\tau)^{\frac{2}{n+2}}. \quad (10)$$

Here, ξ ($\xi = 1/K$), is a constant in the range of 1.0 to 1.1 that depends on the specific heat capacity, E is the energy that is released during the explosion or the absorbed energy per laser pulse, ρ is the gas density, τ is the time delay and n is the shape dependent parameter. The values of n = 1, 2, 3 correspond to planar, cylindrical and spherical shock waves, respectively.

One can use Equation (10) for computation of the blast wave or shock front expansion generated from laser-induced optical breakdown. However, of primary interest is the dependence of the radius,

Preprints (www.preprints.org) | NOT PEER-REVIEWED | Posted: 25 November 2020 doi:10.20944/preprints202011.0652.v1

R(τ), on time delay, τ. Figure 10 displays the maximum of the shock wave radius versus time delay measured perpendicular to the direction of the laser beam propagation. In view of Figures 8 and 9, the maximum is determined from the images near z = 8 mm.

The linear fit (Fig. 10) reveals 0.41 for the slope, or $n = 2.9 \sim 3$. In other words, spherical expansion is inferred. The figure also shows 20% error bars. These error bars are estimated from the variations in the pulse energy for generation of optical breakdown, the trigger-jitter synchronization of the two laser beams (one for plasma generation, the other from a separate device for shadowgraphs), and the readout errors from the displayed images in Figs. 2 to 4. One can also extract from the graph the approximate 1 mm per μs expansion velocity for time delays of ~ 1μs, or Ma = 3. From Equation (10), using ξ = 1.0 to 1.1, E = 800 mJ, ρ = 1.225 kg/m^3 and $n = 3$ yields for the radius $R(\tau$=1 μs) = 3.7 to 4.1 mm, consistent with the measured value of 3.9 mm [4].

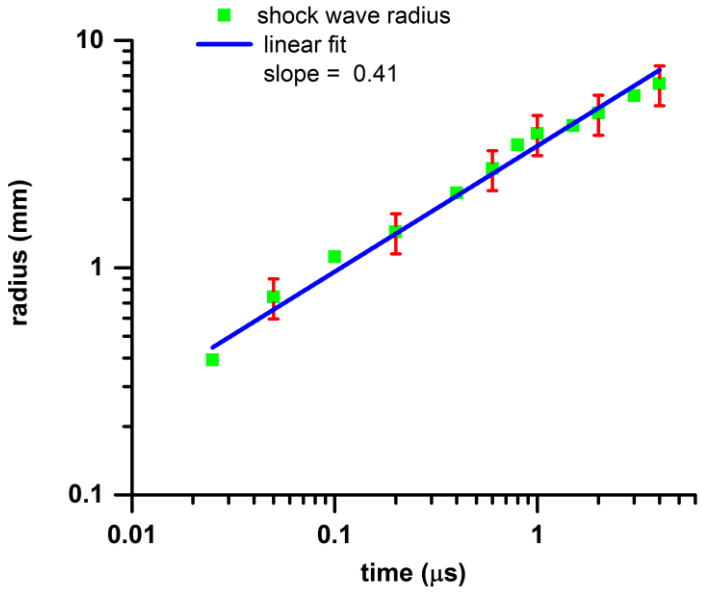

Figure 10. Log-log plot of shock wave expansion measured perpendicular to the laser-propagation direction when using 850-mJ, 6-ns, 1064-nm pulses for optical breakdown in laboratory air [4].

For ultra-high-pure hydrogen, and for time delays of the order of almost 0 to a few dozen ns, recorded spectral images are utilized for exploration of well-above hypersonic expansion. Figure 11 illustrates two images captured from optical breakdown in near atmospheric hydrogen gas, i.e., at a cell pressure of (1.08 ± 0.033) × 10^5 Pa (810 ± 25 Torr).

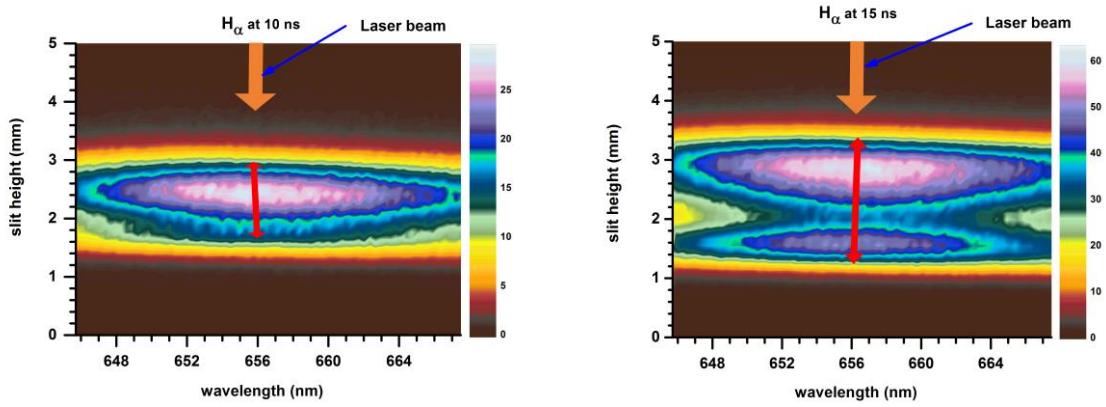

Figure 11. Hydrogen alpha plasma spectra images at 10 ns (left) and 15 ns (right) time delays. The red arrow indicates the measured plasma width [4].

Preprints (www.preprints.org) | NOT PEER-REVIEWED | Posted: 25 November 2020 doi:10.20944/preprints202011.0652.v1

Figure 12 summarizes the expansion speed for early time delays. However, the speed of sound in hydrogen is approximately 4× higher than in air, and the recorded air shadowgraphs can serve as a guide for shockwave appearances. For example, hydrogen expansion at a delay of 400 ns approximately corresponds to air shadowgraphs recorded at a delay of 1600 ns. Most importantly, if the irradiance is not significantly higher than that for optical breakdown thresholds, a spherically symmetric appearance of the shockwave for delays 10× larger than indicated in Figure 12 would be expected analogous to the 170 mJ shadowgraphs recorded in air. Indeed, captured shadowgraphs of optical breakdown in hydrogen [30] reveal a prolate spheroidal shockwave shape for a time delay of 400 ns (see Fig. 1 in Ref. [30]).

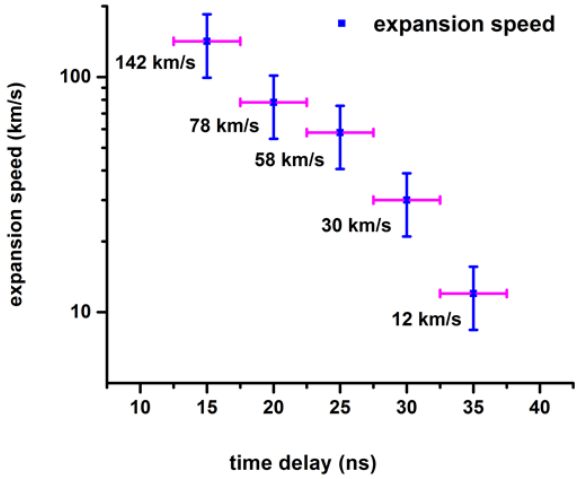

Figure 12. Plasma expansion speeds. The indicated time-delay error bars are due to the gate width of 5 ns [4].

The determined expansion speeds for hydrogen shockwave expansion speeds are well-above hypersonic speed (hypersonic: Ma ≥ 5) or above re-entry speeds (re-entry: Ma ≤ 25) at time delays of 10 to 40 ns.

3.4. Electron Density

Inferred Stark widths of the CI 193.09 nm carbon line in second order for the 1:1 molar CO_2:N_2 gaseous mixture held at atmospheric pressure were determined using the previously discussed peak-fitting Matlab® script [18], deconvolution of the filtered and unfiltered measured peaks, and taking the difference between the filtered and unfiltered deconvoluted peaks.

The inferred Stark widths are plotted versus the slit height of the spectrometer, which can be seen in Figure 13. Larger Stark widths are seen towards the edges of the plasma, while smaller Stark widths are seen in the center of the plasma.

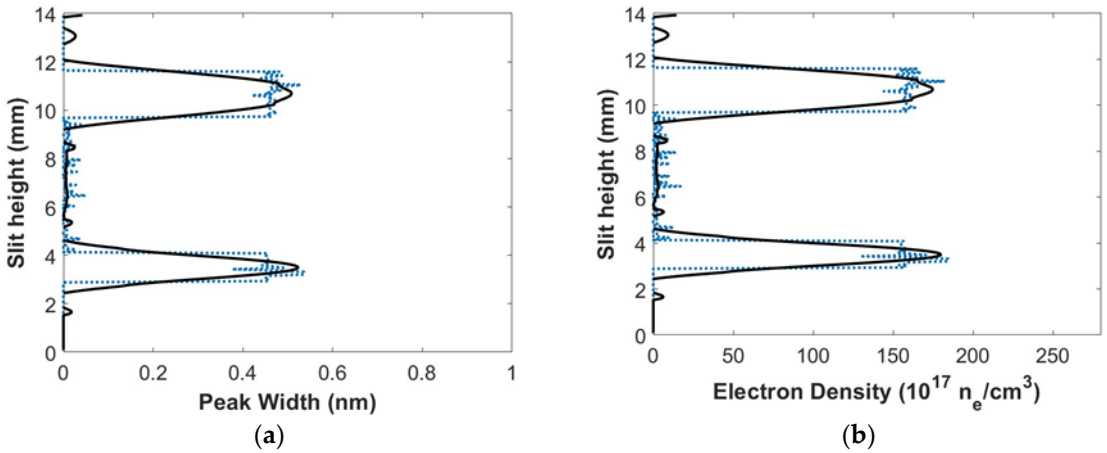

(**a**) (**b**)

Preprints (www.preprints.org) | NOT PEER-REVIEWED | Posted: 25 November 2020 doi:10.20944/preprints202011.0652.v1

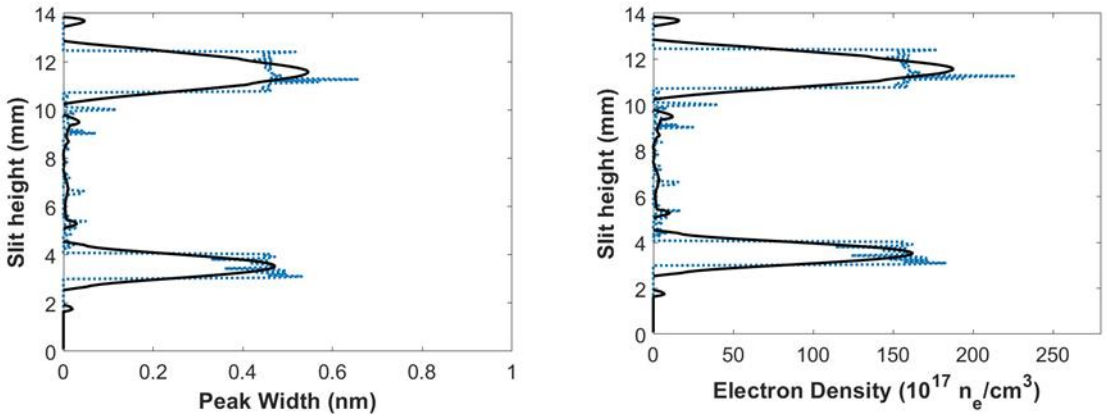

(**c**) (**d**)

Figure 13. Inferred widths and calculated electron densities of C I 193.09 nm atomic carbon line in 2nd order vs. slit height for 1:1 molar CO_2:N_2 gas mixture held at atmospheric pressure. Time delays: (**a**) and (**b**) 450 ns, and (**c**) and (**d**) 950 ns.

For a time delays of 450 and 950 ns, Figs. 13 (a) and (c), the Stark widths are between 0.4 to 0.5 nm and located towards the edges of the plasma. The Stark widths are used to calculate electron number density, n_e. The calculated n_e is plotted versus the slit height of the spectrometer, which can be seen in Figures 13 (b) and (d). Peak electron densities are of the order of $n_e \approx 10^{19}$ cm^{-3}, and values between the two peaks are of the order of $n_e \approx 10^{17}$ cm^{-3}. Since n_e is directly proportional to the Stark width of the 193.09-nm carbon line in second order as previously shown in Equation (5), n_e plots mimic the same behavior as the previously mentioned Stark width plots, where higher n_e is seen towards the edges of the plasma and lower n_e is towards the center of the plasma. The higher electron densities toward the edges of the plasma appear to follow the previously discussed shockwave expansion law, Eq. (1), within the indicated error bars as seen in Table 10.

The Stark shifts of the CI 193.09 nm carbon line in second order for the 1:1 molar CO_2:N_2 gaseous mixture held at atmospheric pressure were also determined using the peak- fitting Matlab® script [18]. Larger Stark shifts are seen towards the edges of the plasma, while smaller Stark widths are seen in the center of the plasma. However, similar results are found when using the Stark shifts, yet with the shock wave fronts more precisely demarcated when using the Stark widths.

Table 10: Computed shockwave radii versus plasma radius for 1:1 molar CO_2:N_2 gaseous mixture held at atmospheric pressure, 170 mJ.

τ (ns)	Computed R(mm)	Measured R_{Plasma}(mm)
450	1.84	2.90 ± 0.87
700	2.20	3.00 ± 0.90
950	2.48	3.30 ± 0.99
1200	2.72	3.35 ± 1.01
1450	2.94	4.00 ± 1.20
1700	3.13	4.30 ± 1.29
1950	3.31	4.40 ± 1.32
2200	3.47	4.30 ± 1.29

3.5. *Cyanide Temperature*

Inferred temperatures of filtered line-of-sight CN spectra in the 1:1 molar CO_2:N_2 gaseous mixture held at atmospheric pressure are plotted versus slit height of the spectrometer as shown in Figure 14. The outgoing shockwave can be seen from time delays of 450 ns to 950 ns. Figure 14 indicates that temperature variations occur in the central region, while increased temperatures are shown at the edges of the plasma. Higher temperatures are seen on the edge of the plasma towards the top of slit or towards the laser side. At a time-delay of 450 ns, Fig. 14 (a), the temperatures in the central region of the plasma are between 9,500 K to 10,000 K, while the temperatures at the edges of

Preprints (www.preprints.org) | NOT PEER-REVIEWED | Posted: 25 November 2020 doi:10.20944/preprints202011.0652.v1

the plasma are more than 10,000 K. At time delays of 950 ns, Fig. 14 (b), the temperatures in the central region of the plasma cool to a range of 9,000 K to 9,500 K, while temperatures at the edges of the plasma are between 9,500 K to 10,000 K. As time elapses further the plasma central region temperatures cool even further to a range of 8,500 K to 9,000 K for time delays of 1.2 μs to 1.7 μs, while the edges of the plasma maintain a temperature range of 9,500 K to 10,000 K. From time delays of 1.95 μs to 2.2 μs, the central region of the plasma sustains temperatures of 8,500 K to 9,000 K and temperatures near the edge of plasma towards the bottom of the slit are around 9,000 K, while temperatures near the edge of the plasma towards the top of the slit increase to greater than 11,000 K.

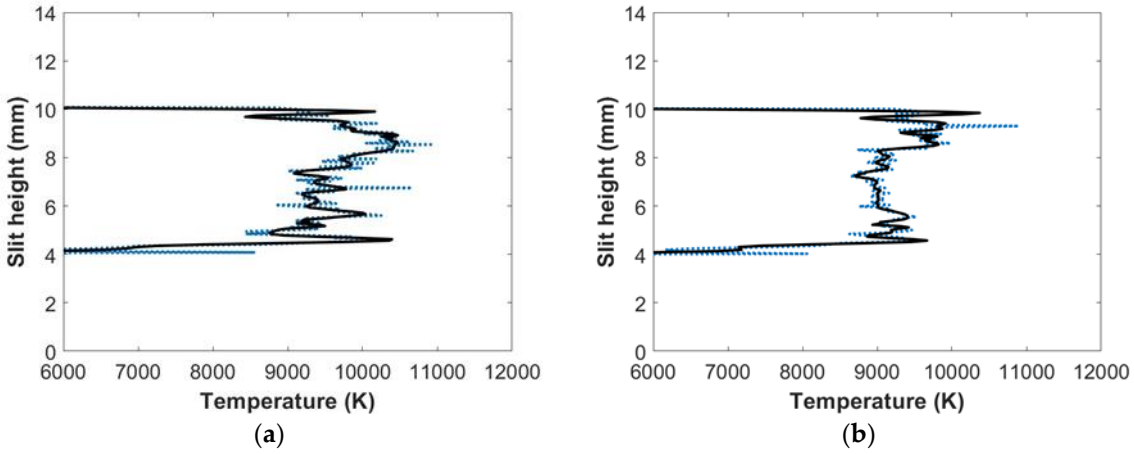

Figure 14. Temperature vs. slit height for filtered line-of-sight CN spectra for fixed volume of 1:1 molar CO_2:N_2 gaseous mixture held at atmospheric pressure. Time delays (**a**) 450 ns; (**b**) 950 ns.

3.6. Abel Inverted Spectra

Abel inversion of the filtered 1:1 molar CO_2:N_2 gaseous mixture held at atmospheric pressure was performed by inverting measured line-of-sight data, I(z, λ), for each wavelength, λ, to obtain the radial emissivity distribution, ε(r, λ). Previously measured shadowgraphs show the plasma generated in the 1:1 molar CO_2:N_2 gaseous mixture held at atmospheric pressure has a close to spherical shape, which would justify the use of Abel inversion.

The irradiance threshold for optical breakdown for the experimental arrangement (see Section 2.1) is ≈ 20 mJ [5], or in terms of irradiance ≈ 3×10^{11} W/cm^2. When using pulse energies of up to about 170 mJ, or up to ≈ 10× breakdown threshold, close to symmetric shock wave expansion occurs. For pulse energies of 800 mJ, or 40 × breakdown threshold, the "symmetric" expansion is seen in the region where most of the energy is absorbed (see Figures 7 and 8).

At a time-delay of 200 ns, Figure 14 (a), the CN distribution appears evenly distributed across the plasma. From time delays of 450 ns to 2200 ns, Figs. 14 (b) and (c) and Fig. 15 (a) to (c), the CN signals begin to become stronger towards the edges of the plasma and weaker in the center of the plasma, which is consistent with the higher temperatures seen at the edges of the plasma as discussed previously. These results were projected to be similar to the shockwave results, but inside the plasma kernel and shockwave the variations of the CN distribution were expected as well.

Preprints (www.preprints.org) | NOT PEER-REVIEWED | Posted: 25 November 2020 doi:10.20944/preprints202011.0652.v1

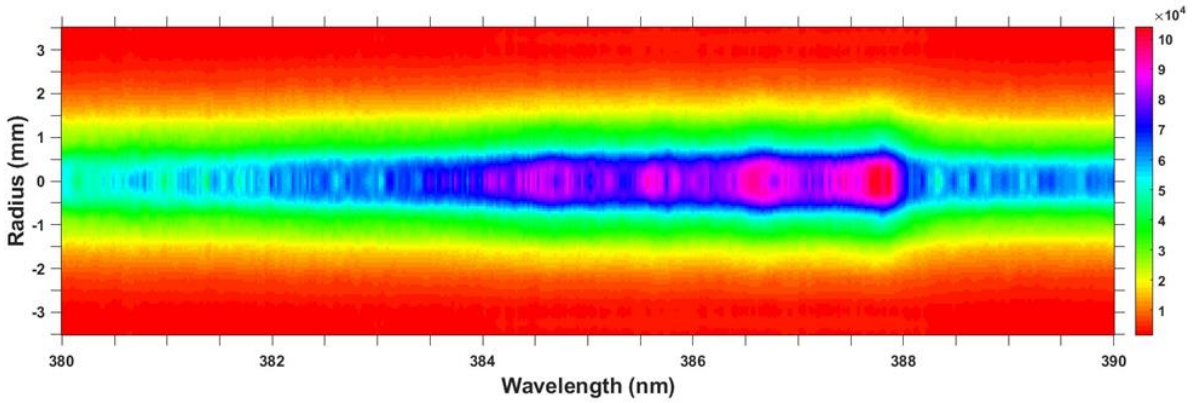

(**a**)

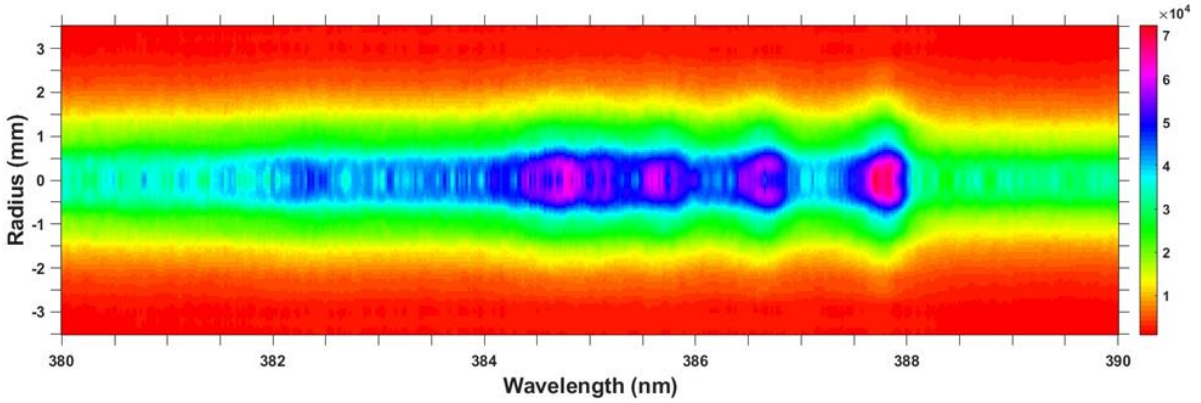

(**b**)

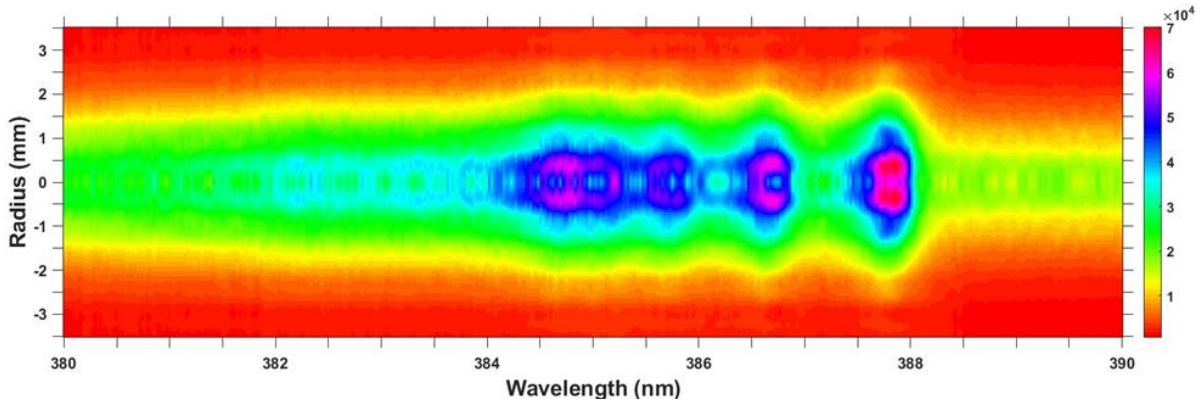

(**c**)

Figure 15. Abel inverted CN spectra 1:1 molar CO_2:N_2 gaseous mixture held at atmospheric pressure. Time delay (**a**) 200 ns; (**b**) 450 ns; (**c**) 950 ns.

Preprints (www.preprints.org) | NOT PEER-REVIEWED | Posted: 25 November 2020 doi:10.20944/preprints202011.0652.v1

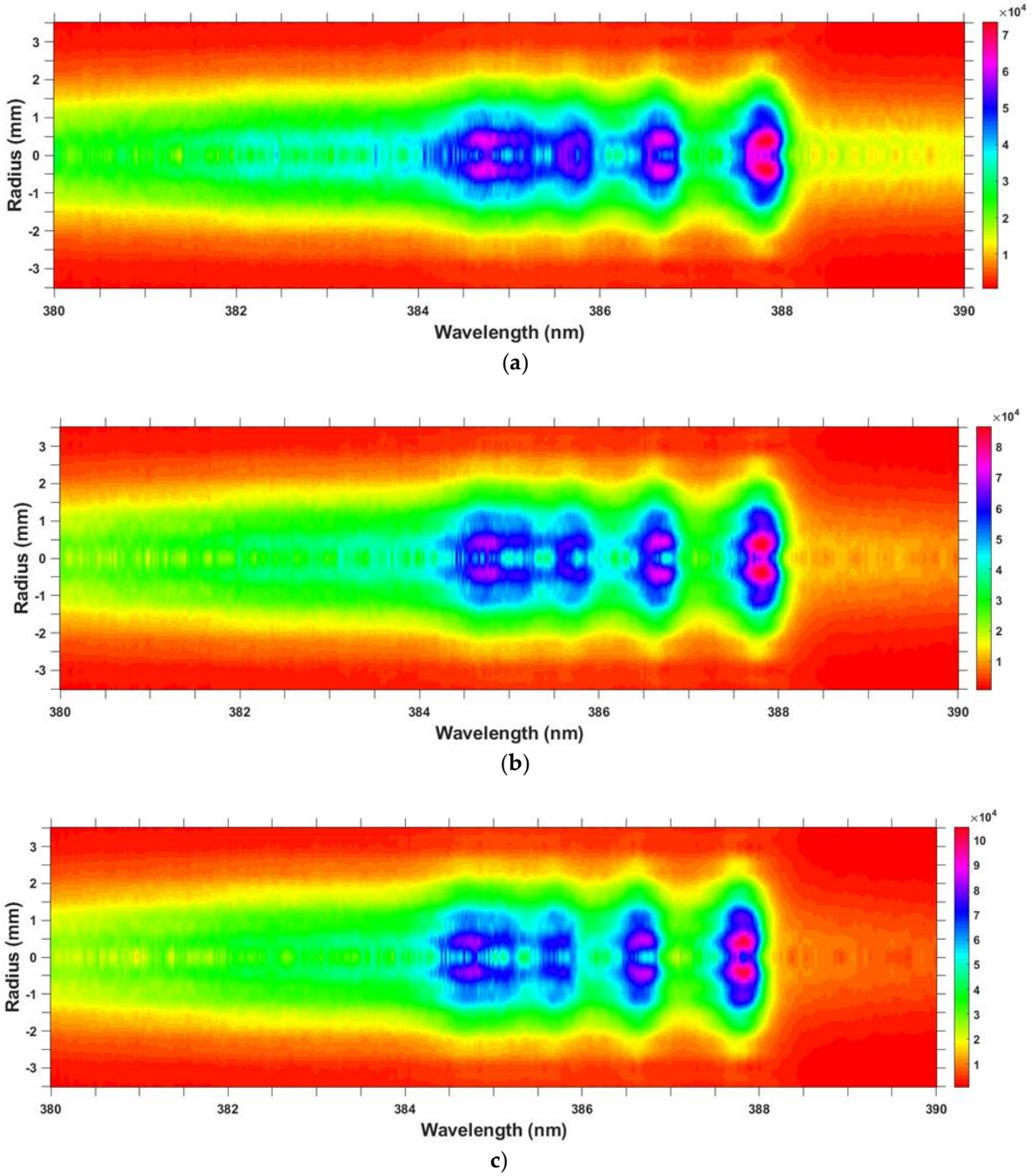

Figure 16. Abel inverted CN spectra 1:1 molar CO_2:N_2 gaseous mixture held at atmospheric pressure. Time delay (**a**) 1200 ns; (**b**) 1700 ns; (**c**) 2200 ns.

4. Discussion and Conclusions

The laser-induced optical breakdown studies of air and selected gases reveal that usually multiple breakdown spots occur along the optical axis when focusing radiation to above threshold irradiance. Once optical breakdown is achieved, the absorbed radiation energy drives the shockwave towards the incoming radiation. The forward cone, or the initial asymmetry noticeable in the shadowgraphs, is a measure of how high above-threshold irradiance is employed.

The species concentration near the shockwave is higher than in the center, especially well developed for time-delays of the order of 1 μs. Both atomic species and diatomic molecular species such as CN indicate consistent results. Moreover, comparison of line-of-sight and of Abel-inverted data show agreement, especially at the spatial location of a breakdown 'bead' closest to the incoming beam one notices the development of the laser-induced plasma that is close to spherical for irradiance

levels about one order of magnitude higher than threshold. For higher irradiances, the shockwave appears to expand into spherical shape towards the laser-side, in agreement with computed spherically expanding shockwaves.

The presented investigations of cyanide formation, especially near the expanding shockwave, are instrumental for potential medical and industrial cyanide diagnosis applications. But clearly, CN detection with LIBS shows the following conclusions:

- Shockwave expansion affects the formation of CN molecules as the plasma expands;
- Stark widths and shifts can be used to determine electron density, but higher spectral resolutions would be desirable for determination of accurate values of electron densities;
- For time delays around 1 μs, higher CN and electron concentrations occur near the shockwave than those in the central region of the plasma. The CN becomes concentrated towards the edges of the plasma, therefore slit size, energy per pulse, and measurement acquisition time would need to be considered when capturing data especially for handheld design;
- The use of a 309 nm cut-on filter is an effective way to filter out unwanted atomic carbon line contributions but causes a ~ 10% reduction in the signal captured, which can cause issues with possible quantification for medical and forensic applications;
- As plasma expands and cools radiation from excited CN molecules seem evenly distributed and indicates a close to homogenous temperature;
- Abel inversion is only justified for radially symmetric light sources, but shadowgraph studies support symmetrization to elucidate spatial dependence.

Author Contributions: All authors contributed equally to this work.

Funding: This research received no external funding.

Acknowledgments: The authors wish to acknowledge the support in part by the Center for Laser Applications at the University of Tennessee Space Institute.

Conflicts of Interest: The authors declare no conflict of interest.

References

1. Miziolek, A., Palleschi, V., Schechter, I., Eds.; *Laser Induced Breakdown Spectroscopy (LIBS): Fundamentals and Applications*. Cambridge University Press, Cambridge, UK, 2006.
2. Singh, J. P., Thakur, S. N., Eds.; *Laser-Induced Breakdown Spectroscopy, 2nd ed.*; Elsevier, Amsterdam, NL, 2020.
3. Gautam, G.; Helstern, C. M.; Drake, K. A.; Parigger, C.G. Imaging of laser-induced plasma expansion dynamics in ambient air. *Int. Rev. At. Mol. Phys.* **2016**, *7*, 45 – 51.
4. Gautam, G.; Parigger, C. G. Plasma Expansion Dynamics in Hydrogen Gas. *Atoms* **2018**, *6*, 46.
5. Parigger, C. G.; Helstern, C. M.; Jordan, B. S.; Surmick, D. M.; Splinter, R. Laser- plasma spatio-temporal cyanide spectroscopy and applications. *Molecules* **2020**, *25*, 615.
6. Helstern, C. M. Laser-Induced Breakdown Spectroscopy and Plasmas Containing Cyanide. PhD Dissertation, University of Tennessee Knoxville, Knoxville, Tennessee, USA, 2020.
7. Cremers, D. A.; Radziemski, L. J. *Handbook of Laser-Induced Breakdown Spectroscopy*. John Wiley and Sons, Hoboken, New Jersey, USA, 2006.
8. Parigger, C. G.; Helstern, C. M.; Gautam, G. Molecular emission spectroscopy of cyanide in laser-induced plasma. *Int. Rev. At. Mol. Phys.* **2017**, *8*, 25 – 35.
9. Bethe, H. A.; Fuchs, K.; Hirschfelder, J. O.; Magee, J. L.; Peierls, R. E.; Neumann, J. *Blastwave*. University of California, Los Alamos, New Mexico, USA, 1947.

10. Taylor, G. I. The formation of a blast wave by a very intense explosion i. Theoretical discussion. *Proc. Math. Phys. Eng. Sci.* **1950,** *201*, 159 – 174.
11. Sedov, L. I. *Similarity and Dimensional Methods in Mechanics*. Academic Press, Cambridge, Massachusetts, USA, 1959.
12. Sedov, L. I. Propagation of strong blast waves. *Prikladnaya Matematika i Mekhanika (Appl. Math. Mech. Leningrad)* **1946**, *10*, 241 – 250.
13. Harith, M. A., Palleschi, V.; Salvetti, A.; Singh, D. P.; Tropiano, G.; Vaselli, M. Hydrodynamic evolution of laser driven diverging shock waves. *Laser Part. Beams* **1990**, *8*, 247 – 252.
14. Parigger C. G.; Helstern, C. M.; Gautum, G. Temporally and spatially resolved emission spectroscopy of cyanide, hydrogen, and carbon in laser-induced plasma. *Atoms* **2019**, *7*, 74.
15. Dackman, M. Laser-Induced Breakdown Spectroscopy for Analysis of High-Density Methane-Oxygen Mixtures. MS Thesis, University of Tennessee Knoxville, Knoxville, Tennessee, USA, 2014.
16. Griem, H. R. *Spectral Line Broadening by Plasmas*. Academic Press, New York, New York, USA, 1974.
17. Surmick, D. M. Spectroscopic Imaging of Aluminum Containing Plasma. PhD Dissertation, University of Tennessee Knoxville, Knoxville, Tennessee, USA, 2016.
18. O'Haver T. *peakfit.m.* Available online: https://www.mathworks.com/matlabcentral/fileexchange/23611-peakfit-m (accessed on May 22, 2019).
19. Parigger, C. G.; Hornkohl, J. O. *Quantum Mechanics of the Diatomic Molecule with Applications.* IOP Publishing, Bristol, UK, 2019.
20. Parigger, C. G.; Woods, A. C.; Surmick, D. M.; Gautam, G.; Witte, M. J.; Hornkohl, J.O. Computation of diaotmic molecular spectra for selected transitions of aluminum monoxide, cyanide, diatomic carbon, and titanium monoxide. *Spectrochim Acta Part B: At. Spectrosc.* **2015**, *107*, 132 – 138
21. Nelder, J. A.; Mead, R. A simplex-method for function minimization. *Comput. J.* **1965**, *7*, 308 – 313.
22. Pretzler, G. A new method for numerical Abel-inversion. *Z. Naturforsch. A* **1991**, *46*, 639 – 641.
23. Pretzler, G.; Jäger, H.; Neger, T.; Philipp, H.; Woisetschläger, J. Comparison of different methods of Abel inversion using computer simulated and experimental side-on data. *Z. Naturforsch. A* **1992**, *47*, 955 – 970.
24. Kandel, Y. P. An experimental study of hydrogen Balmer lines in pulsed laser plasma. PhD Dissertation, Wesleyan University, Middletown, Connecticut, USA, 2009.
25. Gornushkin, I. B.; Shabanov, S. V.; Panne, U. Abel inversion applied to a transient laser induced plasma: implications from plasma modeling. *J. Anal. At. Spectrom.* **2011**, *26*, 1457 – 1465.
26. Killer, C. Abel inversion algorithm. Available online https://www.mathworks.com/matlabcentral/fileexchange/43639-abel-inversion-algorithm (accessed on June 30, 2019).
27. Parigger, C. G.; Gautam, G.; Surmick, D. M. Radial electron density measurements in laser-induced plasma from Abel inverted hydrogen Balmer beta line profiles. *Int. Rev. At. Mol. Phys.* **2015**, *6*, 43 – 57.
28. Gautam, G. On Laser-induced Plasma Containing Hydrogen. PhD Dissertation, University of Tennessee Knoxville, Knoxville, Tennessee, USA, 2017.
29. Parigger, C. G.; Surmick, D. M.; Gautam G. Self-absorption characteristics of measured laser-induced plasma line shapes. *J. Phys.: Conf. Ser.* **2017**, *810*, 012012.
30. Gautam, G.; Parigger, C. G.; Helstern, C. M.; Drake, K. A. Emission spectroscopy of expanding laser-induced gaseous hydrogen-nitrogen plasma. *Appl. Opt.* **2017**, 56, 9277 – 9284.
31. Dardis, J.; Costello, J.T. Stagnation layers at the collision front between two laser-induced plasmas: A study using time-resolved imaging and spectroscopy. *Spectrochim. Acta Part B: At. Spectrosc.* **2010**, *65*, 627 – 535.
32. Zel'dovich, Ya. B., Raizer Yu. P. *Physics of Shock Waves and High-Temperature Hydrodynamic Phenomena, Volume 1*. Hayes W. D., Probstein, R. F., Eds., Academic Press, New York, NY, USA, 1966; pp. 347 – 348.